

Coronal hydrodynamics of laser-produced plasmasA. Aliverdiev,^{1,2} D. Batani,² R. Dezulian,² T. Vinci,^{2,3} A. Benuzzi-Mounaix,³ M. Koenig,³ and V. Malka⁴¹*Institute of Physics of Daghestan Scientific Center of Russian Academy of the Science, 367003, Russia,**Daghestan, Makhachkala, 94 Yaragskogo Street*²*Dipartimento di Fisica “G. Occhialini,” Università di Milano-Bicocca, Milan, Italy*³*Laboratoire pour l’Utilisation des Lasers Intenses, Ecole Polytechnique, Palaiseau, France*⁴*Laboratoire d’Optique Appliquee, Ecole Polytechnique, Palaiseau, France*

(Received 30 March 2008; published 27 October 2008)

We present the results of an experimental investigation of the temporal evolution of plasmas produced by high power laser irradiation of various types of target materials (at intensities $I_L \leq 10^{14}$ W/cm²). We obtained interferometric data on the evolution of the plasma profile, which can directly be compared to analytical models and numerical simulations. For aluminum and plastic targets, the agreement with 1D simulations done with the hydrocode MULTI is excellent, at least for large times ($t \geq 400$ ps). In this case, simulations also show that the effect of radiation transport is negligible. The situation is quite different for gold targets for which, in order to get a fair agreement, radiation transport must be taken into account.

DOI: [10.1103/PhysRevE.78.046404](https://doi.org/10.1103/PhysRevE.78.046404)

PACS number(s): 52.50.Jm, 52.38.-r, 52.70.-m, 52.65.-y

INTRODUCTION

The investigation of the hydrodynamics of laser-produced plasmas is fundamental for several areas of physics, including inertial confinement fusion (ICF). In ICF, laser beams are focused on a solid spherical pellet. Laser ablation creates plasma, which expands in vacuum, producing an extended corona, which affects laser propagation. On the other side, due to momentum conservation, the plasma expansion sets the conditions for the inward propagating shock, which drives the implosion of the pellet.

Although several theoretical models of plasma expansion have already been developed [1–3] and many experiments have been conducted, still there are not many “clean” experimental results. Indeed, most previous experiments were strongly influenced by two-dimensional (2D) effects of plasma expansion, either because the focal spot was quite small compared to the expansion size, or because the irradiation profile was not uniform, but characterized by hot spots.

In recent years, several optical smoothing techniques have been introduced to eliminate the problem of large-scale hot spots. In particular some of these techniques, such as phase zone plates [4] (PZPs), allow the production of flat-top intensity profiles. In this case, one fundamental experimental parameter, the laser intensity on target, is clearly defined. This is not the case with the usual Gaussian-like intensity distribution or, even worse, with typical focal spots affected by hot spots. Having a new flat-top profile and a well-defined intensity allows a well-characterized study of plasma expansion. Also, 2D effects may be strongly reduced by using of PZPs and large focal spots, thus producing a situation which is much closer to that described by one-dimensional (1D) theoretical models (the other condition assumed in such 1D self-similar analytical models is that laser irradiation is constant in time, which nowadays can also be met thanks to laser pulse shaping capabilities).

In recent experiments the progress in plasma characterization has been made by using diagnostic techniques based on

x-ray laser [5], which allow measurements of higher plasma density. Nevertheless, the use of streak cameras in combination with optical interferometers gives both a good temporal resolution and reconstruction of the plasma profile, that were the key points of our work.

Finally let us notice that another very important aspect in the understanding of plasma hydrodynamical expansion is the contribution of radiation (XUV) transport [6,7]. In our experiments this could be tested by using targets with different atomic numbers and therefore different radiative properties. A clear modeling of plasma expansion and of the role of radiation transport during expansion are clearly key issues in the physics of inertial confinement fusion (ICF) driven by lasers.

I. EXPERIMENTAL SETUP

The experiment was realized at the LULI laboratory using two beams from the Nd:glass high power laser system converted to 2ω and together delivering a typical intensity of 10^{14} W/cm² on target. The temporal profile is approximately trapezoidal with rise and fall time of 150 ps and a flat top duration of 600 ps. The spot diameter produced by the lens coupled to the phase zone plates had a full width at half maximum (FWHM) of 400 μ m with central flat top region of 200 μ m diameter. A probe beam (Nd:YAG laser converted to 2ω) was coupled to Mach-Zehnder interferometer and to a streak-camera with ps resolution. The diagnostic system allowed the evolution of the plasma density profile to be measured as a function of time (Fig. 1).

Also, in our experiment, different targets (CH₂, Al, Au) with different radiative properties were used. In particular plasma expansion with Au targets should be strongly influenced by radiation (XUV) transport [6,7], while, in the case of CH₂ targets, energy transport should be determined by electrons only.

II. EXPERIMENTAL RESULTS

Figure 2 shows typical streak camera images obtained for our three different target materials. Image size is 375 μ m

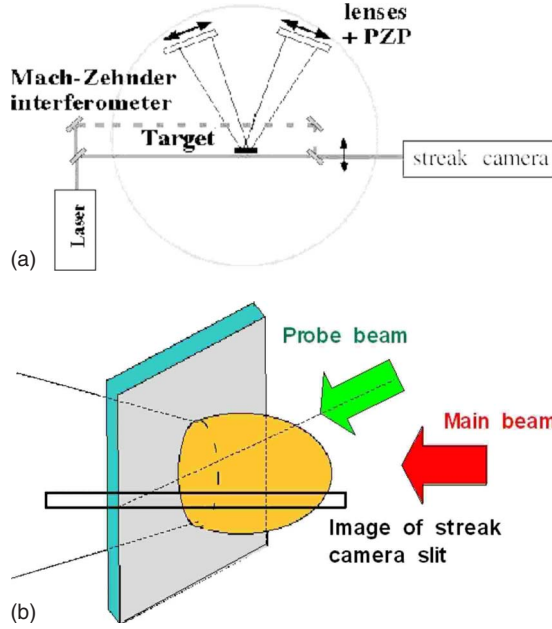


FIG. 1. (Color online) (a) Sketch of the experimental setup. (b) Principle of the experiment.

(horizontal scale) and 1.065 ns (vertical scale) in all cases. Here x_1 represents the shadow of the target in the image plane. Initially the fringes are stationary because there is no plasma expansion. At the time t_1 they begin to move, first close to the target surface and at larger and larger distances.

Figure 3 presents streak camera images obtained for four other shots and they have been introduced to show not only the effect of changing the laser intensity (for instance, compare Fig. 2(a) with Figs. 3(a) and 3(b), and compare Fig. 2(c) with Figs. 3(c) and 3(d) but also the good reproducibility of our experimental results. [The sweep time for shots No. 2 and No. 3 was originally different but here the images have been stretched to yield the same sweep speed.]

The plasma-induced phase shift in a point x of the interferometric picture is

$$\Delta\phi_{\text{plasma}}(x,t) = \frac{2\pi}{\lambda} \left(L - \int_{-L/2}^{L/2} n(x,y,t) dy \right), \quad (1)$$

where λ is the wavelength of the laser beam, L the effective plasma length, and n the plasma refractive index.

In the approximation of 1D plasma expansion (i.e., no dependence on radial distance, or on coordinate y) and assuming the usual expression for the plasma refraction index, we get

$$\Delta\phi_{\text{plasma}}(x,t) = \frac{2\pi L}{\lambda} \left(1 - \sqrt{1 - \frac{n_e(x,t)}{n_c}} \right), \quad (2)$$

where

$$n_c = \frac{4\pi^2 c^2 \epsilon_0 m_e}{\lambda^2 e^2} \quad (3)$$

is the critical density for the probe beam (equal to $3.9 \times 10^{21} \text{ cm}^{-3}$), and n_e is the free electrons density. If $n_e \ll n_c$, then $\frac{\lambda \Delta\phi_{\text{plasma}}}{2\pi L} \approx [1 - (1 - \frac{1}{2} \frac{n_e}{n_c})]$, i.e., $\frac{\lambda \Delta\phi_{\text{plasma}}}{\pi L} = \frac{n_e}{n_c}$. Hence

$$N = \frac{L}{n_c \lambda} n_e, \quad (4)$$

where $N = \Delta\phi/\pi$ is the number of π -phase shifts in the interferometric streak-camera images.

Notice that experimental data directly give the value of N and not n_e . In order to recover the value of the electronic density we need to know the plasma size L , whose value will be discussed later in the paper [8,9].

III. RESULTS AND DISCUSSION

Figure 4 shows the experimental dependences of N vs x at various fixed times t obtained from streak camera images and plotted in a semilog plot (solid lines). Here time is measured starting from the time t_1 at which the fringes in the image begin to move (however, this is not a critical choice: we could as well use the initial time of the streak camera image). We see that such curves are well interpolated by straight (dashed) lines, i.e., by exponential profiles.

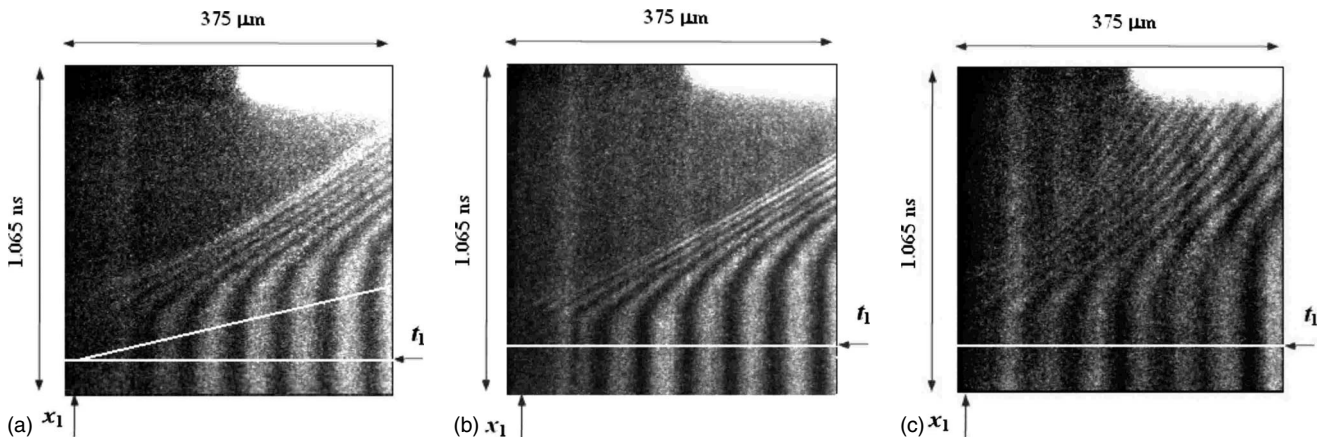


FIG. 2. Interferograms recorded with the streak camera (a) Al (shot 5, $E=49.6$ J), (b) CH_2 plastic (shot 6, $E=51.3$ J), (c) Au (shot 7, $E=54.4$ J). Image size is $375 \mu\text{m}$ (horizontal scale) and 1.065 ns (vertical scale) for all images. Vertical arrows show the position x_1 , horizontal arrows the time t_1 . The white line in Fig. 2(a) represents the ensemble of the points where the fringes begin to move.

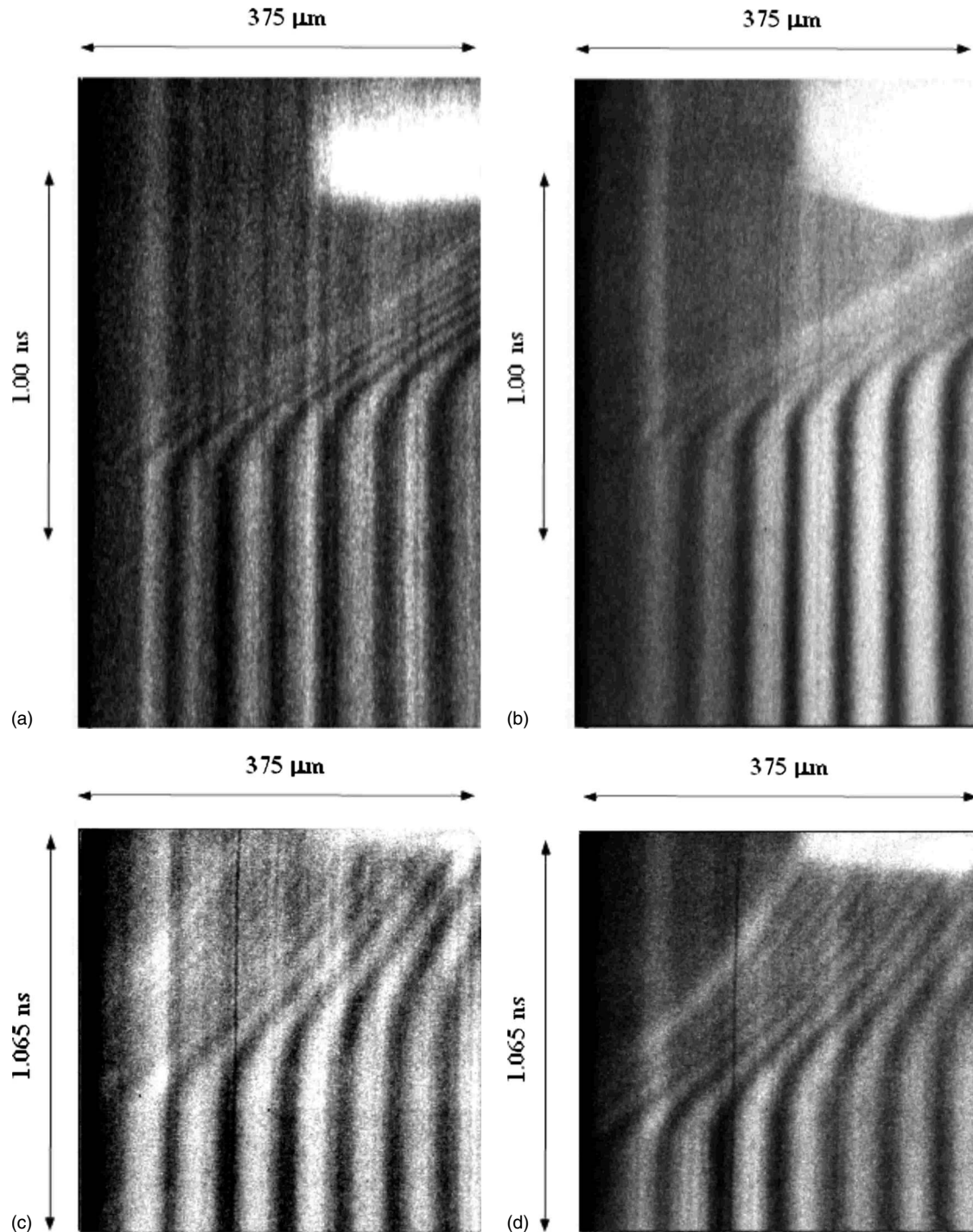


FIG. 3. Interferograms recorded with the streak camera: (a) Al (shot 2, $E=42.7$ J), (b) Al (shot 3, $E=67.6$ J), (c) Au (shot 9, $E=59.7$ J), (d) Au (shot 10, $E=51.5$ J). Image horizontal scale is $375 \mu\text{m}$ for all images. Vertical scale is 1.736 ns for (a) and (b) and 1.065 ns for (c) and (d).

The fact that the profile is exponential is in a good agreement with theoretical 1D self-similar models of plasma expansion [1–3] according to which

$$n_e(x,t) = n_c \exp\left(-\frac{(x-x_0)}{c_s(t-t_0)}\right), \quad (5)$$

where

$$c_s = 9.79 \times 10^5 \sqrt{\frac{\gamma Z^* T_e}{\mu}} \quad (6)$$

in cm/s is the adiabatic sound velocity, γ the adiabatic constant ($\gamma=1$ if electrons are isothermal), μ the atomic number, and Z^* is the ionization degree, which can, for instance, be calculated with the formula by Colombant and Tonon [10],

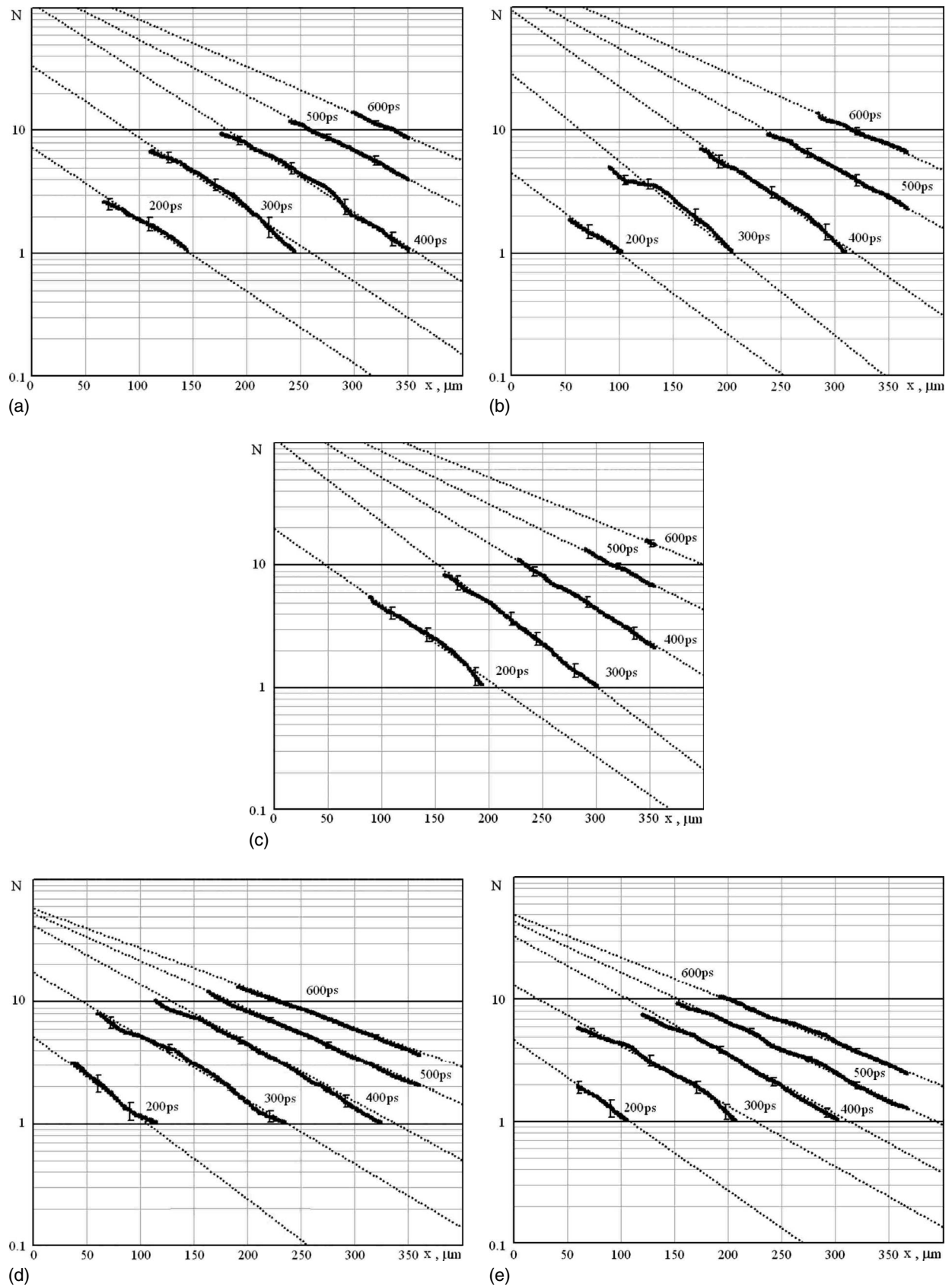


FIG. 4. Experimental profiles obtained from the interferograms in Fig. 2 in semilog plot and their interpolations by exponential curves (straight lines), (a) Al shot No. 5, (b) Al shot No. 2, (c) CH₂ shot No. 6, (d) Au shot No. 7, (e) Au shot No. 10. Typical error bars are also shown in the figures (at late times the size of the error bars is comparable with the marker size so it cannot be seen in the graph).

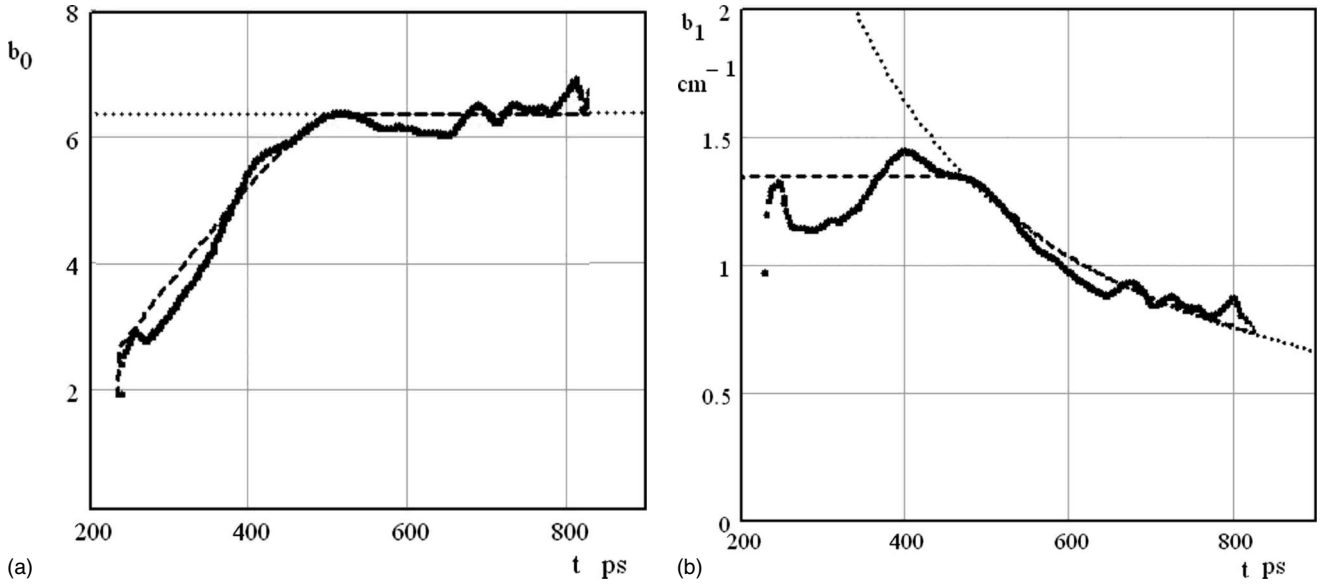


FIG. 5. Values of b_0 and b_1 obtained from the analysis of experimental data of Al shot No. 5 (solid curve), a smooth fit to the data (dashed line), and the case of constant b_0 and c_s (dotted lines).

which is valid in collisional-radiative equilibrium conditions. T_e is the electron temperature in eV, which in classical models (where energy is absorbed at the critical surface in the plasma and transported inward by electronic conduction) is typically given by $T_e(\text{eV})=10^{-6} (I_L \lambda^2)^{2/3}$, where I_L in W/cm^2 is the laser beam intensity, and λ is in μm .

Here t_0 marks the beginning of the laser-target interaction (when the laser pulse reaches the target front side), and x_0 is the initial position of the solid surface [exactly x_0 should correspond to the actual position of the critical surface, which moves inward the target due to the ablation of the material; however because the ablation velocity is much smaller (more than one order of magnitude) than the sound velocity, we can neglect the time dependence of x_0 in Eq. (5) than the sound velocity we can neglect the time dependence of x_0 in Eq. (5)].

Formula (5) corresponds to

$$N(x,t) = \frac{L}{\lambda} \exp\left(-\frac{(x-x_0)}{c_s(t-t_0)}\right). \quad (7)$$

Let us notice that in all interferometric streak-camera images we see the shadow of the target (position x_1). However, if there is a small tilt of the target (~ 2 mm large), then the position of the focal spot does not correspond to x_1 but to $x_1 \approx x_0 - L \tan(\theta)$, where θ is the angle between the target plane and a probe beam. For $L \approx 1$ mm and $\theta \sim 6^\circ$ we find $x_1 - x_0 \approx 100 \mu\text{m}$. This implies that the value of x_0 is not directly accessible from our data. However, it can be estimated from the intersection point of the interpolation lines in Fig. 3. Indeed, it is possible to show that all the lines corresponding $t > 400$ ps intersect around $x_0 \approx -100 \mu\text{m}$.

Once x_0 is known, the time t_0 is found by extrapolating the line at which the fringes begin to move [the white inclined line in Fig. 1(a)] back to the position x_0 . By shifting the origin of the coordinates to (x_0, t_0) , we can then write Eq. (6) as

$$\ln[N(x,t)] = b_0 - b_1 x, \quad (8)$$

where $b_1 = (\frac{1}{c_s t})$ and $b_0 = \ln(\frac{L}{\lambda})$.

Now, fitting from our experiment results for $N(x,t)$ and using the least square method, we find the time dependences of b_0 and b_1 , as shown in Figs. 5(a) and 5(b) (solid lines). The dashed lines give a smooth interpolation of such time dependences. More precisely, the curve for b_0 [Fig. 5(a)] is obtained by using a least square fit method of data after assuming the smooth interpolation of the coefficient b_1 presented in Fig. 5(b).

The dotted lines in Figs. 5(a) and 5(b) correspond to the theoretical expectation $b_0 = \text{const}$ and $b_1 = 1/[c_s(t - \Delta t_0)]$, where Δt_0 is an addition time-shift, which is physically related to the fact that the temporal profile of the laser pulse is trapezoidal rather than flat-top (see the Appendix). The constant value of b_0 determines the plasma length though the relation $L = \lambda \exp(b_0)$.

The value L , found from b_0 for Al (shot No. 5) corresponds to an average plasma length $L = \lambda \exp(b_0) \sim 315 \mu\text{m}$. This is in fair agreement with our expectation from the focal spot size (FWHM $\sim 400 \mu\text{m}$ with a $\sim 200 \mu\text{m}$ flat top central region). Very similar behaviors (and the practically the same value of L) are found for all other shots for Al and plastic targets.

We notice that the value of c_s obtained from experimental data perfectly corresponds to the calculated sound velocity in Table I (let us notice that here we made no attempt to adjust

TABLE I. Summary of laser shots (experimental data).

N	Target	Pulse energy (J)	I_L (10^{13} W/cm 2)	c_s (10^7 cm/s)	b_0
2	Al	42.7	4.0	1.72	6.38
3	Al	67.6	7.2	2.00	6.38
5	Al	49.6	5.3	1.81	6.38
6	CH $_2$	51.3	5.5	1.84	6.38
7	Au	54.4	5.7	1.96	4.70
9	Au	59.7	6.3	2.00	4.70
10	Au	51.5	5.5	1.88	4.70

the laser intensity in order to force a good agreement between experimental data and calculated values).

The comparison of experimental interferogram (for Al, shot No. 5) with the synthesized interferogram calculated from the smooth interpolation of experimental b_0 and b_1 is

presented in Fig. 5(a), and, as expected, shows a perfect agreement. If, instead, we use the behavior $b_0 = \text{const}$ and $c_s = \text{const}$, i.e., the dotted lines in Figs. 5, we get the synthesized interferogram shown in Fig. 6(b) which, at early time, is slightly different from the experimental result.

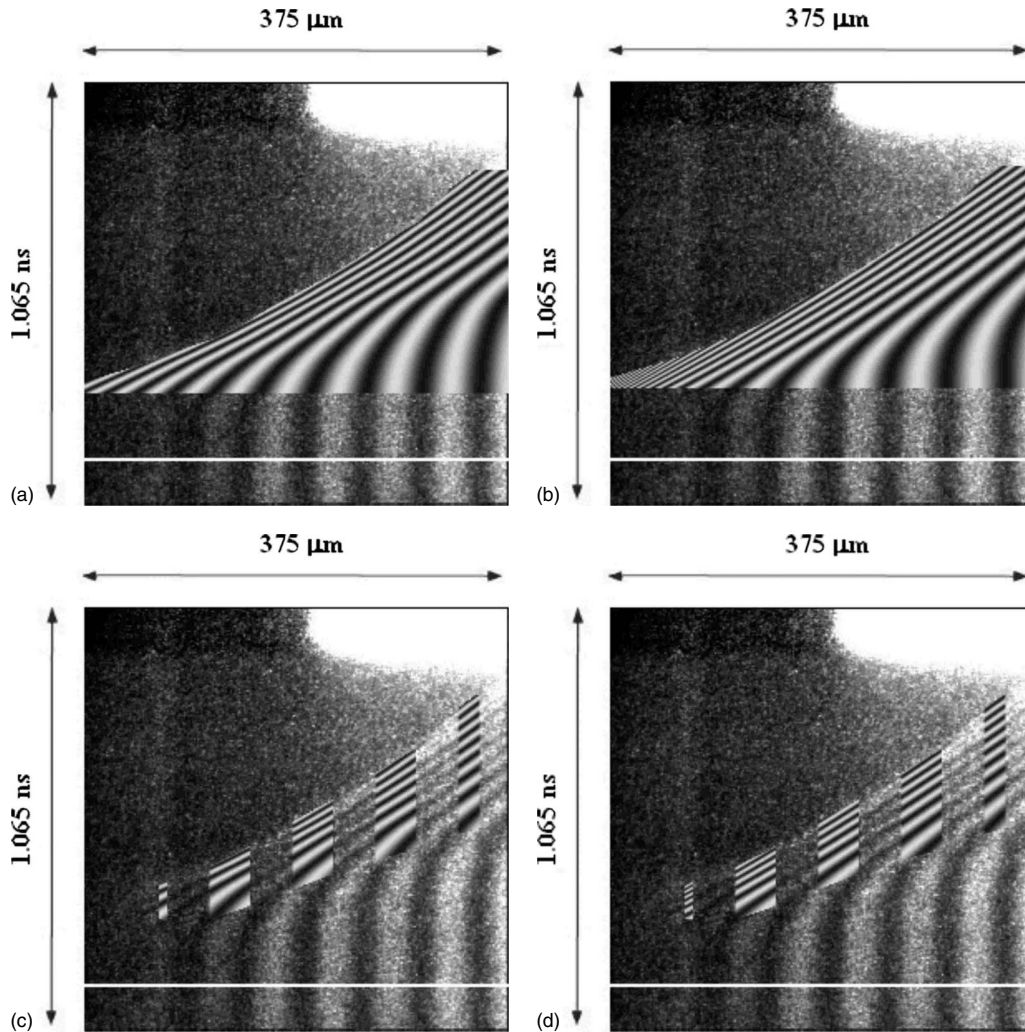


FIG. 6. Synthesized interferograms (top) and comparison with experimental ones (bottom) for Al shot No. 5: (a) b_0 and b_1 from the smooth fit in Fig. 5; (b) constant b_0 and c_s . The total image dimensions are $375 \mu\text{m}$ (horizontal scale) and 1.065 ns (vertical scale) for all images. On the bottom the images show, in alternate stripes, the experimental interferograms and synthesized ones.

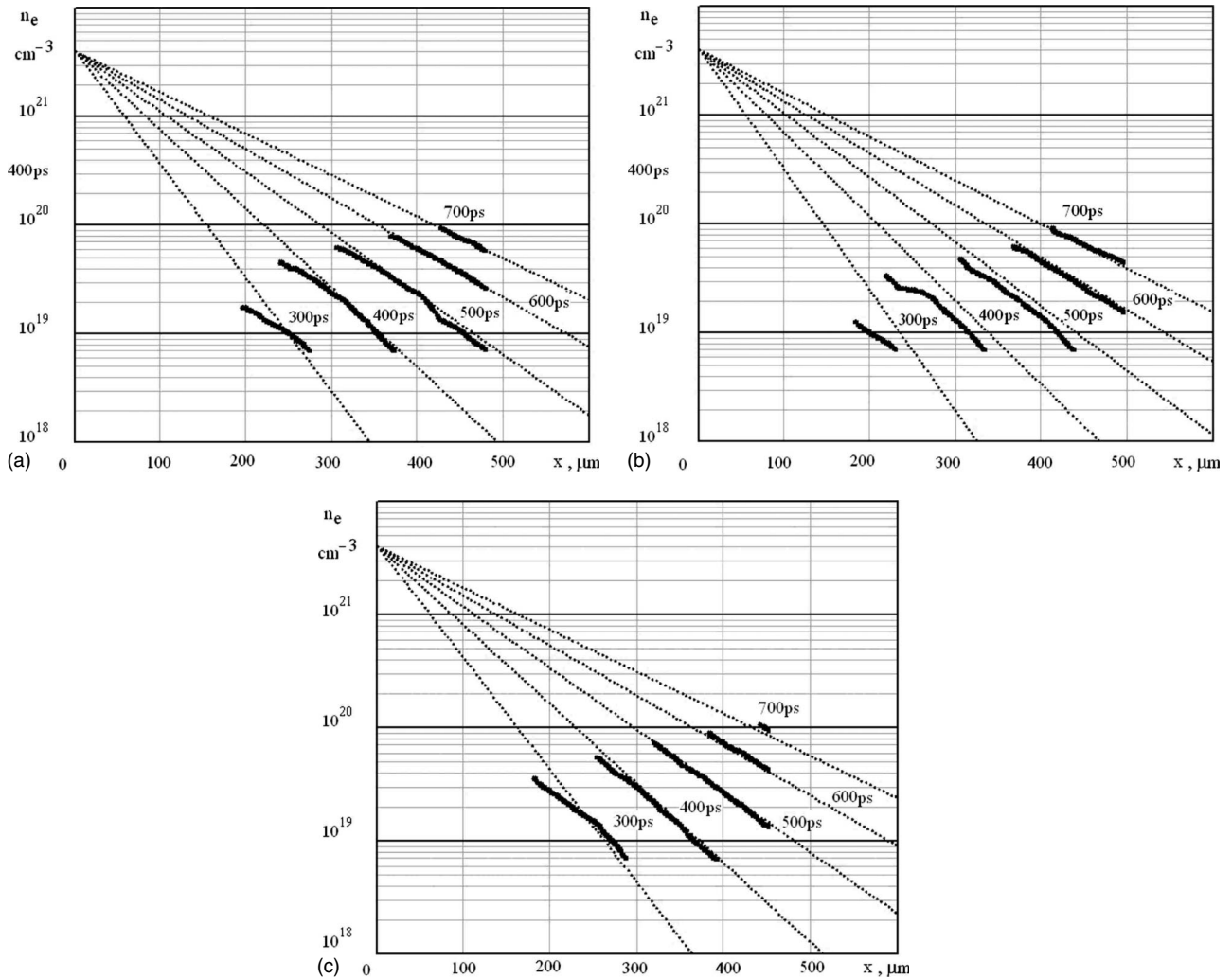


FIG. 7. Comparison of experimental profiles with the predictions of the analytic 1D model; (a) Al shot No. 5; (b) Al shot No. 2; (c) CH₂ shot No. 6.

IV. COMPARISON OF CH₂ AND Al RESULTS WITH ANALYTICAL 1D MODEL AND WITH HYDRO SIMULATIONS

Let us first discuss Al and CH₂ data, which due to the low atomic number, should not be affected by radiation transport. Results obtained with Au targets will be presented later in the paper. In Fig. 7 we report the experimental density profiles (solid lines) and the comparison with the 1D analytic model with the parameters L and c_s obtained as described before. We can see that in all cases we can experimentally access the region up to $n_e = 10^{20} \text{ cm}^{-3}$, i.e., $1/40$ of the critical density. We also see that the theoretical predictions are well verified for $t > 400 \text{ ps}$, which is the density profile is well reproduced by an exponential slope, using the calculated parameters L and c_s .

In order to refine our analysis, we also compared our experimental results to numerical simulations performed using the 1D hydrocode MULTI (multigroup radiation transport in multilayer foils) [11]. Simulations performed for the case of Al target (shot No. 5) are reported in Figs. 8(a) and 8(b) with (a) and without (b) radiation transfer respectively. Both local

temperature equilibrium (LTE) and non-LTE opacities have been obtained from an average hydrogenic model implemented in the code SNOP [12–14]. We used flux limiter with the usual value $f=0.06$, which is well known to reproduce experimental results.

We can see that in the case of Al and plastic targets the effect of radiation transport is practically negligible (a conclusion which was somewhat implicit in the good agreement with the analytical model, which of course does not include radiation transport). Also, we see that the MULTI simulations for the aluminum and plastic targets are in excellent agreement with our experimental data, again for large times ($t > 400 \text{ ps}$).

For shorter times, the agreement is not perfect. Probably, in this case nonlocal transport, radiation transport (including non-LTE opacities), etc., combine to produce deviations from analytical and flux-limited numerical predictions as recently shown in Refs. [15,16]

V. ANALYSIS OF GOLD RESULTS

Data for Au targets have been analyzed following the same procedure of Al and CH data. The time dependences of

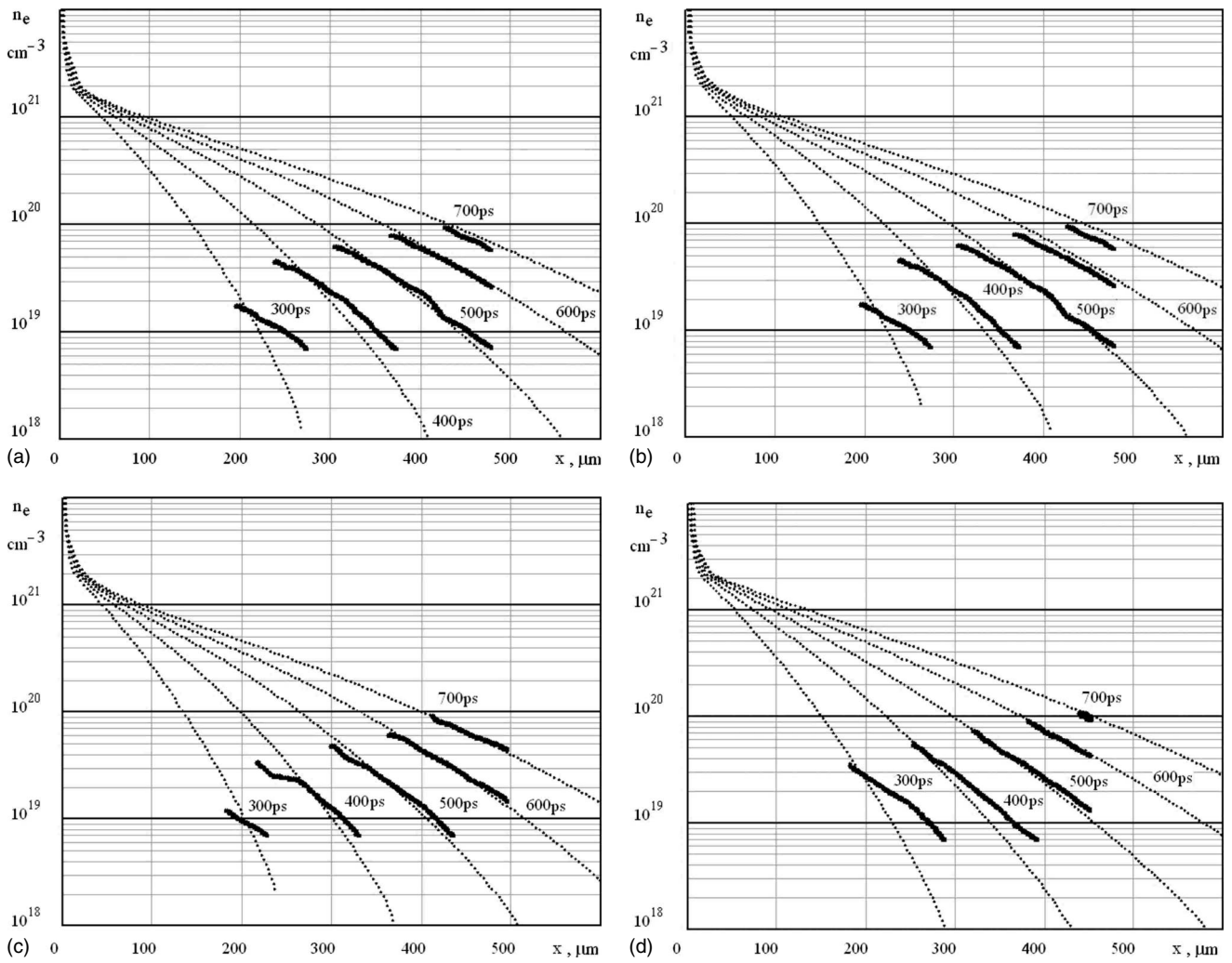


FIG. 8. Comparison of experimental profiles with the results of MULTI simulations; (a) Al shot No. 5 radiative, (b) Al shot No. 5 nonradiative, (c) Al shot No. 2 nonradiative, (d) CH₂ shot No. 6 nonradiative.

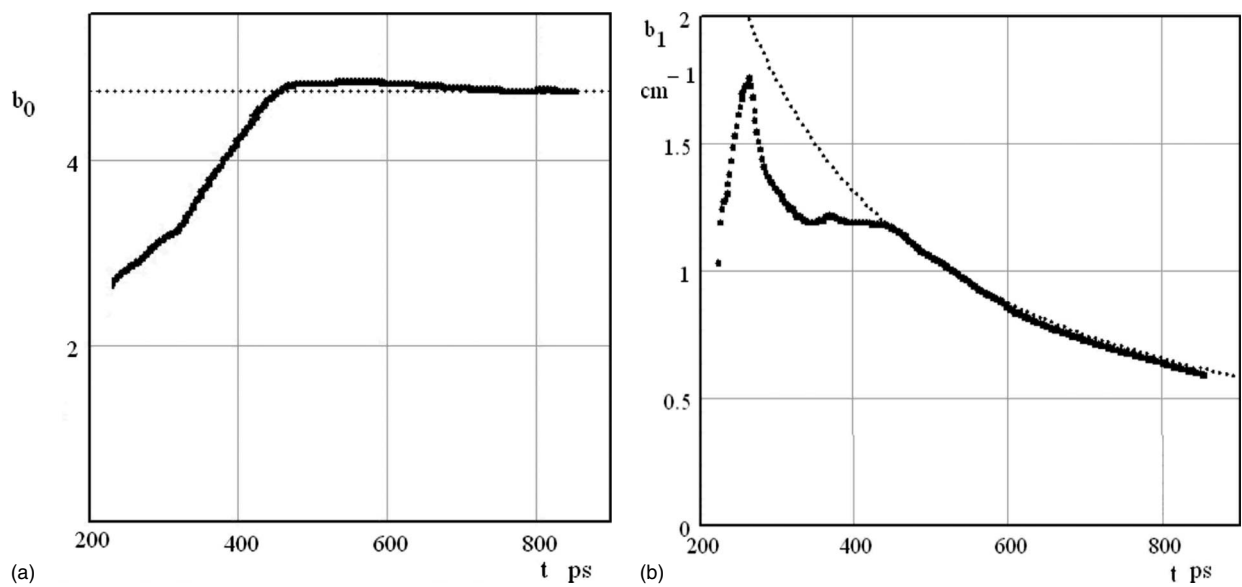


FIG. 9. Values of b_0 and b_1 obtained from the analysis of experimental data for gold target (solid curve) and the case of constant b_0 and c_s (dotted lines).

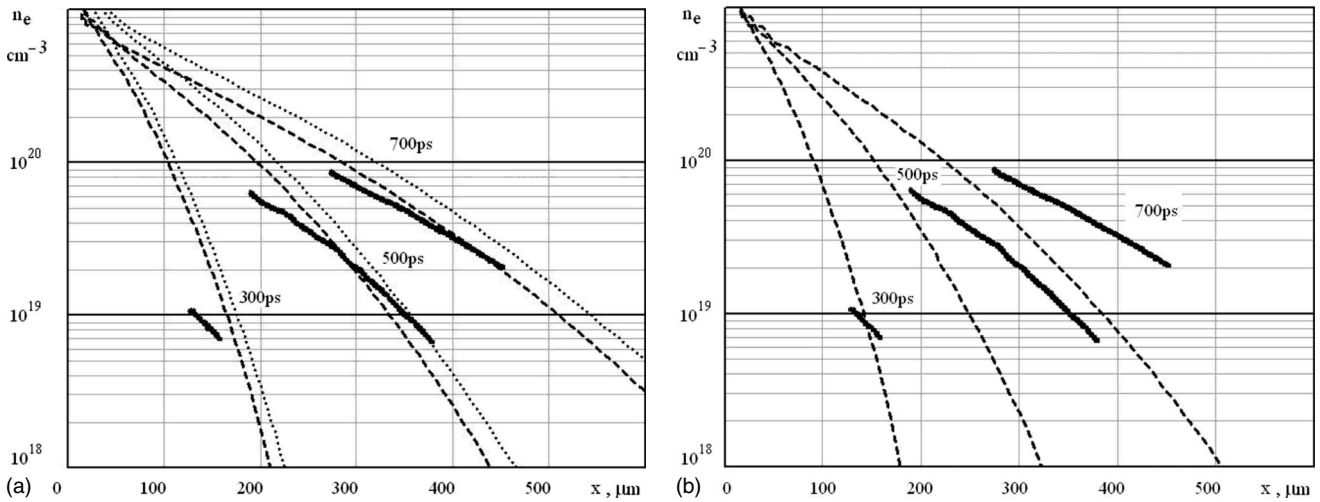


FIG. 10. Results of multisimulations for gold targets and comparison with experimental data. Dotted lines have been obtained without radiative transfer, dashed lines with radiative transfer, (a) with LTE opacities and (b) with non-LTE opacities. [For clarity, only three different times are shown.]

coefficients b_0 and b_1 from Fig. 3 are presented in Fig. 9 (solid lines). The dotted line in Figs. 9(a) and 9(b) corresponds to the theoretical expectation $b_0 = \text{const}$ and $b_1 = 1/[c_s(t - \Delta t_0)]$, where $\Delta t_0 = 60$ ps. The time behavior of b_0 and b_1 is the same of that previously reported for Al and CH, although the numerical value of b_0 is not the same. However, for the calculations of the electron density in Fig. 10 we still have used the plasma length value of $315 \mu\text{m}$.

Figure 10 shows the results of MULTI 1D simulations for gold targets, with (dashed lines) and without (dotted lines) radiative transfer, and the comparison to the experiment (Au, shot No. 7). We can see that in this case radiation transport is important. However, even with radiative transfer, the agreement between experimental data and simulations results is not as good as that for aluminum or plastic targets, especially for initial times and close to the target surface. Figure 10(b) shows the results of simulations with non-LTE opacities. We see that for the short times the agreement with radiative

transfer is slightly better, although not perfect, while the situation reverses for longer times.

This probably shows that non-LTE effects are important at early times, while later the situation becomes much closer to LTE conditions. In both cases, the nonperfect agreement may probably be explained by the fact that, since radiation transport is important in this case, a better description of opacities would also be important.

CONCLUSIONS

Our experiment data have been obtained with laser irradiation conditions, which were approximately flat top in space and in time and free from hot spots. Therefore we could obtain interferometric data on the evolution of the plasma electronic profile, which can directly be compared to 1D analytical models and numerical simulations. The agreement is excellent at least for large times ($t \geq 400$ ps). In the

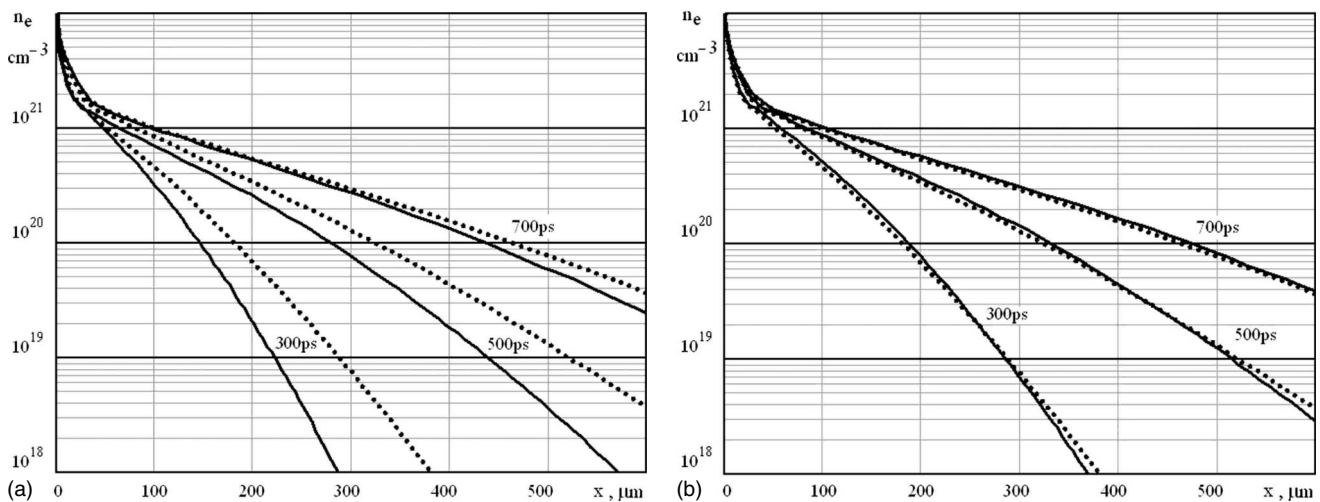


FIG. 11. (a) Results of simulations for Al shot No. 5 for a flat-top temporal profile (solid lines) and for a trapezoidal profile with rise and fall time of 150 ps (dotted lines); (b) the same data where now the results for the trapezoidal case have been shifted by $\Delta t_0 = 60$ ps.

case of Al and plastic targets, simulations also show that the effect of radiation transport is completely negligible (at least in the plasma corona region we can access, i.e., $n_e < n_c/40$).

The situation is quite different for gold targets. In this case there is a significant difference with and without radiation transport. The agreement is not perfect, which probably implies the need for a better description of LTE and non-LTE plasma opacities.

ACKNOWLEDGMENTS

The authors warmly acknowledge the help of the LULI technical staff for the realization of this experiment and of Professor Hem Chandra Pant for the discussion. A.A. is also grateful to Landau Network–Centro Volta–Cariplo Foundation and to INTAS (Grant No. 06-1000014-5638).

APPENDIX

The additional time shift Δt_0 is related to the temporal shape of the laser pulse, which is trapezoidal rather than flat top. This can be shown by looking at the results of the numerical MULTI simulations. Figure 11(a) compares the re-

sults of simulations with the same total pulse energy and the same target parameters (correspondents to Al target, shot No. 5), but with different temporal profiles. The solid lines represents the results for a flat-top temporal profile, the dotted lines represent the results for a trapezoidal profile with rise and fall time of 150 ps.

Figure 11(b) shows the same data where now the results for the trapezoidal case have been shifted by $\Delta t_0=60$ ps (the value which we have recovered from all our experimental data). We can see that in this case, the results from the two cases are very close to each other. Simulations for different laser intensity and target material practically yield the same result.

Such time $\Delta t_0=60$ ps is very close to the value of 75 ps which corresponds to half of the laser-pulse rise time (actually they are equal within the experimental error bars). Therefore we can understand this result by saying that, at large times, i.e., for times larger than the laser pulse rise time t_R , a laser pulse increasing in time over t_R will give the same hydrodynamical profiles of a constant laser pulse, starting at a time $t_R/2$ later (in this way the two pulses contain the same energy in their initial phase)

-
- [1] C. E. Max *et al.*, Phys. Fluids **23**, 1620 (1980).
 [2] W. M. Manheimer, D. G. Colombant, and J. H. Gardner, Phys. Fluids **25**, 1644 (1982).
 [3] P. Mora, Phys. Fluids **25**, 1051 (1982).
 [4] M. Koenig, B. Faral, J. M. Boudenne, D. Batani, A. Benuzzi, and S. Bossi, Phys. Rev. E **50**, R3314 (1994).
 [5] D. Ress *et al.*, Science **265**, 514 (1994).
 [6] R. Sigel *et al.*, Phys. Rev. Lett. **65**, 587 (1990).
 [7] N. Kaiser, J. Meyer-ter-Vehn, and R. Sigel, Phys. Fluids B **1**, 1747 (1989).
 [8] A. Aliverdiev *et al.*, in *24th International Symposium on Rarefied Gas Dynamics*, edited by M. Capitelli, AIP Conf. Proc. No. 762 (AIP, Melville, 2005), p. 419.
 [9] A. Aliverdiev *et al.*, in *3rd International Conference on Super-strong Fields in Plasmas*, edited by M. Lontano and D. Batani, AIP Conf. Proc. No. 827 (AIP, Melville, 2006), p. 540.
 [10] G. F. Tonon and D. Colombant, J. Appl. Phys. **44**, 3524 (1973).
 [11] R. Ramis, R. Schmalz, and J. Meyer-Ter-Vehn, Comput. Phys. Commun. **49**, 475 (1988).
 [12] K. Eidmann, Laser Part. Beams **12**, 223 (1994).
 [13] K. Eidmann, W. Schwanda, I. Foeldes, R. Sigel, and G. D. Tsakiris, J. Quant. Spectrosc. Radiat. Transf. **51**, 77 (1994).
 [14] G. D. Tsakiris and K. Eidmann, J. Quant. Spectrosc. Radiat. Transf. **38**, 353 (1987).
 [15] G. Gregori *et al.*, Phys. Rev. Lett. **92**, 205006 (2004).
 [16] D. R. Gray and J. D. Kilkenny, Plasma Phys. **22**, 81 (1980).